Inhibition of temperature runaway phenomenon in the Sabatier process using bed dilution structure: LBM-DEM simulation

Yixiong Lin[a], Chen Yang[b], Cheolyong Choi[a], Wei Zhang[c], Kazui Fukumoto[a], Hiroshi Machida[a], Koyo Norinaga[a,*]

[a]Department of Chemical Systems Engineering, Graduate School of Engineering, Nagoya University, Furo-cho, Chikusa-ku, Nagoya 464-8603, Aichi, Japan

[b]College of Chemical Engineering, Fuzhou University, Fuzhou 350116, Fujian, China

[c]College of Mechanical and Transportation Engineering, China University of Petroleum-Beijing, Beijing 102249, China

Correspondence author: norinaga@nagoya-u.jp (K. Norinaga)

Abstract

The Sabatier process is promising for carbon dioxide utilization and energy storage. However, the serious problem that limits more comprehensive industrial applications is catalyst deactivation due to the temperature runaway phenomenon. The inert particle dilution approach, including the mixing dilution method and layered dilution method is applied to solve this problem. Based on the lattice kinetic scheme-lattice Boltzmann method (LKS-LBM), the effects of three parameters in bed dilution structure reconstructed by the discrete element method (DEM) on temperature distribution and carbon conversion rate were discussed, so as to investigate the relationship between packing structure and temperature distribution. Furthermore, numerical results indicated that an optimal bed dilution structure, which not only can control the peak temperature below the critical temperature to avoid coking and sintering of catalyst, but also can improve the carbon conversion rate by almost 18% compared with the

structure without dilution under the same circumstance.

Keywords: Sabatier Process, Bed Dilution, Temperature Runaway Phenomenon, Lattice Boltzmann Method, Discrete Element Method

Introduction

The Sabatier process is a promising process for carbon dioxide utilization and energy storage due to the ever-increasing greenhouse effect and energy demands. The Sabatier reaction converts H_2 and CO_2 into combustible gas with high energy density, CH_4:

$$4H_2 + CO_2 \rightleftharpoons CH_4 + 2H_2O \quad \Delta H_R^{298K} = -165 \; kJ \cdot mol^{-1} \tag{1}$$
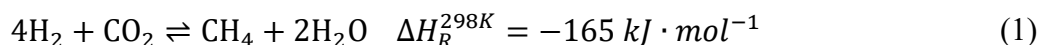
Eq. (1) indicates that the Sabatier process refers to a strongly exothermic reaction. High-temperatures cause a sintered catalyst with carbon deposition on its surface. As a result, those result in catalyst deactivation, one of the most severe industrial applications problems. I.e., the temperature runaway phenomenon is still challenging to tackle the Sabatier process.

Most studies[1-5] mentioned that the reasonable reaction temperature range for the Sabatier process is 533-823 K. The Sabatier process is an exothermic reaction and thermodynamically favored at low temperatures. However, at low temperatures, the kinetic limitation would reduce the conversion efficiency of CO_2 to CH_4[6]. Conversely, relatively high temperatures cause catalyst deactivation, as mentioned above. Therefore, temperature control plays an important role in the Sabatier process. Several previous studies mainly focused on synthesizing the catalyst that keeps high activity and stability at low temperatures[6-9]. Transitional metal-based and noble metal-based catalysts have been successively synthesized and have made notable progress so far. Plus, some literature highlighted that high temperatures over 823 K easily

deactivated the catalysts by sintering and carbon deposition, which should be avoided[2-3].

Therefore, controlling the peak temperature in the Sabatier process is still important.

In order to further optimize the Sabatier process's temperature distribution, especially for the temperature runaway phenomenon, the optimization of catalysts packing structure should be studied. Industrial utilization often employs a fixed bed reactor for the Sabatier process[10-12]. Regarding structure optimization in a fixed bed reactor, Berger et al.[15] reported that different bed reactor configurations could affect the axial and radial dispersion of reactants in heterogeneous catalytic reactions. Guo et al.[13] developed a novel type of fixed bed structure with the radial layered configuration. They used a wire mesh to split the reactor into two parts in the radial direction to enhance radial heat conduction. Hong et al.[14] optimized the packing structure in the fixed bed reactor by adding inert particles to regulate temperature distribution and reaction conversion for Fischer-Tropsch synthesis (FTS). As they reported, adding inert particles is capable of effectively regulating the temperature distribution, as well as increasing CO_2 conversion and CH_4 selectivity compared with the case without inert particles. Regarding the Sabatier process, few studies involve optimizing the catalysts packing structure to solve the temperature runaway phenomenon

The present study is aimed to investigate the fluid flow, heat and mass transport, and chemical reaction in the packing structure by virtue of the bed dilution. The discrete element method (DEM) is adopted to reconstruct a pellets' random packing structure computationally (e.g., catalyst particle and inert particle). The effects of three parameters in bed dilution structure on temperature distribution and carbon conversion rate are explored, which are volume fraction of inert particle, inert particle dilution method, inert particle conductivity,

respectively. Moreover, the lattice kinetic scheme-lattice Boltzmann method (LKS-LBM) model is adopted to simulate the Sabatier process in bed dilution structure, so as to obtain an optimal bed dilution configuration.

Numerical Simulation Method

General description

The present study investigates heterogeneous reactions and transport in porous media. Fig. 1 shows a schematic diagram of this process. The transport in porous media contains two parts: inter-particle convective heat and mass transport and intra-particle heat and mass transport. The inter-particle transport occurs in the void of porous media, which includes external diffusion, convection, and surface adsorption. In contrast, the intra-particle transport occurs inside the catalyst particles, including the intra-particle diffusion and intra-particle adsorption. Typically, the heterogeneous reactions occur inside the catalyst[57]. However, the present study assumes a homogeneous reaction on particle surface for simplicity, following the previous studies[53-55].

Based on the description of reaction and transport in porous media, the governing equations are expressed as follows:

$$\nabla \cdot (\rho \mathbf{u}) = 0 \qquad\qquad in \ V \qquad\qquad (2)$$

$$\nabla \cdot (\rho \mathbf{u}\mathbf{u}) = -\nabla p + \nabla \cdot (\nabla \mu \mathbf{u}) \qquad in \ V_F \qquad (3)$$

$$\nabla \cdot (\mathbf{u}C_i) = \nabla \cdot (D_i \nabla C_i) + S_i \qquad in \ V_F \qquad (4)$$

$$\nabla \cdot (\mathbf{u}T) = \nabla \cdot \left(\frac{\lambda}{\rho C_p}\nabla T\right) + S_T \qquad in \ V \qquad (5)$$

where $\mathbf{u}$, p, C_i, T, λ, C_p are the local velocity vector, pressure, concentration of ith component, temperature, thermal conductivity, heat capacity, respectively. V is the total

volume, whereas V_F is the fluid volume around catalyst particles. S_i and S_T are the source terms related to reaction kinetics and reaction heat, respectively.

Compared with other numerical methods, the lattice Boltzmann method (LBM) has several advantages in dealing with porous media. The LBM is a mesoscopic computational fluid dynamics (CFD) method, which can flexibly handle irregular boundary conditions in porous media and is not limited by the fluid continuity assumption. Extensive studies[19-23] have affirmed the LBM approach. Therefore, the present study adopted the LBM to solve the above governing equations.

Lattice Boltzmann solver for fluid flow equation

The multiple-relaxation-time (LBM-MRT) model has several advantages in numerical stability, accuracy, and efficiency. The evolution of the LBM-MRT equation is as follows:

$$f_\alpha(\mathbf{x} + \mathbf{e}_\alpha \Delta t, t + \Delta t) - f_\alpha(\mathbf{x}, t) = -(\mathbf{M}^{-1}\mathbf{S}_F\mathbf{M})[f_\alpha(\mathbf{x}, t) - f_\alpha^{eq}(\mathbf{x}, t)] \tag{6}$$

where $f_\alpha(\mathbf{x}, t)$ is the particle velocity distribution function at position $\mathbf{x}$ and time t; $\mathbf{e}_\alpha$ is the αth discrete velocity. In the present study, the D3Q15 discrete velocity model[60] was adopted for three-dimension fluid flow calculation as seen in Fig. 2. $\mathbf{M}$ and $\mathbf{S}_F$ are the transformation matrix and a diagonal relaxation matrix, respectively. $f_\alpha^{eq}(\mathbf{x}, t)$ is the equilibrium distribution function. According to He and Luo[24] $f_\alpha^{eq}(\mathbf{x}, t)$ can be given by:

$$f_\alpha^{eq}(\mathbf{x}, t) = w_\alpha \left\{ \rho + \rho_0 \left[\frac{\mathbf{e}_\alpha \cdot \mathbf{u}}{c_s^2} + \frac{(\mathbf{e}_\alpha \cdot \mathbf{u})^2}{2c_s^4} - \frac{\mathbf{u}^2}{2c_s^2} \right] \right\} \tag{7}$$

where w_α is the weight coefficient; c_s is the lattice sound speed. Notably, ρ is a variable related to the pressure as $p = c_s^2\rho$, and ρ_0 denotes the density of the fluid. For the D3Q15 discrete velocities model, $\mathbf{e}_\alpha$, c_s, w_α, $\mathbf{M}$, $\mathbf{S}_f$ are given by:

$$\mathbf{e}_0=(0,0,0),$$

$$\mathbf{e}_1=(1,0,0), \ \mathbf{e}_2=(-1,0,0), \ \mathbf{e}_3=(0,1,0),$$

$$\mathbf{e}_4=(0,-1,0), \ \mathbf{e}_5=(0,0,1), \ \mathbf{e}_6=(0,0,-1), \tag{8}$$

$$\mathbf{e}_7=(1,1,1), \ \mathbf{e}_8=(-1,1,1), \ \mathbf{e}_9=(1,-1,1), \ \mathbf{e}_{10}=(-1,-1,1),$$

$$\mathbf{e}_{11}=(1,1,-1), \ \mathbf{e}_{12}=(-1,1,-1), \ \mathbf{e}_{13}=(1,-1,-1), \ \mathbf{e}_{14}=(-1,-1,-1)$$

$$c_s = 1/\sqrt{3}, \ w_0=2/9, \ w_{1\text{-}6}=1/9, \ w_{7\text{-}14}=1/72 \tag{9}$$

$$\mathbf{M}=\begin{bmatrix}
1 & 1 & 1 & 1 & 1 & 1 & 1 & 1 & 1 & 1 & 1 & 1 & 1 & 1 & 1 \\
-2 & -1 & -1 & -1 & -1 & -1 & -1 & 1 & 1 & 1 & 1 & 1 & 1 & 1 & 1 \\
16 & -4 & -4 & -4 & -4 & -4 & -4 & -4 & 1 & 1 & 1 & 1 & 1 & 1 & 1 \\
0 & 1 & -1 & 0 & 0 & 0 & 0 & 1 & -1 & 1 & -1 & 1 & -1 & 1 & -1 \\
0 & -4 & 4 & 0 & 0 & 0 & 0 & 1 & -1 & 1 & -1 & 1 & -1 & 1 & -1 \\
0 & 0 & 0 & 1 & -1 & 0 & 0 & 1 & 1 & -1 & -1 & 1 & 1 & -1 & -1 \\
0 & 0 & 0 & -4 & 4 & 0 & 0 & 1 & 1 & -1 & -1 & 1 & 1 & -1 & -1 \\
0 & 0 & 0 & 0 & 0 & 1 & -1 & 1 & 1 & 1 & 1 & -1 & -1 & -1 & -1 \\
0 & 0 & 0 & 0 & 0 & -4 & 4 & 1 & 1 & 1 & 1 & -1 & -1 & -1 & -1 \\
0 & 2 & 2 & 0 & -1 & -1 & -1 & -1 & 0 & 0 & 0 & 0 & 0 & 0 & 0 \\
0 & 0 & 0 & 1 & 1 & -1 & -1 & 0 & 0 & 0 & 0 & 0 & 0 & 0 & 0 \\
0 & 0 & 0 & 0 & 0 & 0 & 0 & 1 & -1 & -1 & 1 & 1 & -1 & -1 & 1 \\
0 & 0 & 0 & 0 & 0 & 0 & 0 & 1 & 1 & -1 & -1 & -1 & -1 & 1 & 1 \\
0 & 0 & 0 & 0 & 0 & 0 & 0 & 1 & -1 & 1 & -1 & -1 & 1 & -1 & 1 \\
0 & 0 & 0 & 0 & 0 & 0 & 0 & 1 & -1 & -1 & 1 & -1 & 1 & 1 & -1
\end{bmatrix} \tag{10}$$

$$\mathbf{S}_f = diag\left(1, 1.2, 1.2, 1, s_q, 1, s_q, 1, s_v, s_v, s_v, s_v, s_v, 1.98\right) \tag{11}$$

1   Note that the parameters in the relaxation matrix are normally in the range of 0 to 2. The values

2   of s_q and s_v are related to the mixture kinematic viscosity (v_{mix}):

$$v_{mix} = c_s^2\left(\frac{1}{s_v}-\frac{1}{2}\right)\Delta t, \ s_q = \frac{16s_v-8}{8s_v-1} \tag{12}$$

3   According to the Chapman-Enskog expansions, density (ρ) and velocity vector (**u**) can be

4   defined by:

$$\rho = \sum_\alpha f_\alpha \tag{13}$$

$$\rho\mathbf{u} = \sum_\alpha \mathbf{e}_\alpha f_\alpha \tag{14}$$

Lattice Boltzmann solver for heat and mass transport equation

The Bhatnagar-Gross-Krook (BGK) model is the most widely used model for heat and mass transport. Based on the numerous previous studies[25-28], however, the numerical accuracy and stability of the BGK model depend strongly on the relaxation time in the evolution equation. The relaxation times for heat (τ_h) and mass (τ_g) transport are determined by the thermal diffusion coefficient and mass diffusion coefficient, respectively. In the lattice Boltzmann equation, the relaxation times can be defined:

$$\tau_g = \frac{D}{c_s^2 \Delta t} + 0.5 = \frac{Ma}{Pe_M} \frac{L}{c_s \Delta t} + 0.5 \tag{15}$$

$$\tau_h = \frac{k}{c_s^2 \Delta t} + 0.5 = \frac{Ma}{Pe_T} \frac{L}{c_s \Delta t} + 0.5 \tag{16}$$

where $Ma = \frac{U}{c_s}$, $Pe_M = \frac{UL}{D}$ and $Pe_T = \frac{UL}{k}$ are the Mach number, the Péclet number for mass transport, the Péclet number for heat transport, respectively. Moreover, U and L are the characteristic velocity and the reference length. As indicated in Eqs. (10) and (11), it can be easily deduced that τ_g and τ_h approach to 0.5 with an increase in Pe_M and Pe_T, respectively, resulting in a numerical instability problem as pointed out by Sterling and Chen[29]. In order to improve stability, one can increase the value of L. However, this treatment will require to refine the lattice. Hence, it would cost massive computer resources and significantly reduce computational efficiency. Inamuro used the lattice kinetic scheme (LKS) was used to solve the instability problem without refining the lattice[36]. The LKS evolution equations for mass and heat transport with D3Q7 velocity discrete model are as below:

$$g_a^i(\mathbf{x} + \mathbf{e}_\alpha \Delta t, t + \Delta t) - g_a^i(\mathbf{x}, t) = -\frac{1}{\tau_g}\left[g_a^i(\mathbf{x}, t) - g_a^{i(eq)}(\mathbf{x}, t)\right] + w_a S_i \tag{17}$$

$$g_\alpha^{i(eq)} = w_\alpha C_i\left[1 + \frac{\mathbf{e}_\alpha \cdot \mathbf{u}}{c_{s,i}^2}\right] + w_\alpha A_i \Delta t(\mathbf{e}_\alpha \cdot \nabla C_i) \tag{18}$$

$$h_\alpha(\mathbf{x} + \mathbf{e}_\alpha \Delta t, t + \Delta t) - h_\alpha(\mathbf{x}, t) = -\frac{1}{\tau_h}\left[h_\alpha(\mathbf{x}, t) - h_\alpha^{eq}(\mathbf{x}, t)\right] + w_a S_T \tag{19}$$

$$h_\alpha^{eq} = w_\alpha T \left[1 + \frac{\mathbf{e}_\alpha \cdot \boldsymbol{u}}{c_{s,i}^2}\right] + w_a A_T \Delta t (\mathbf{e}_\alpha \cdot \nabla T) \tag{20}$$

1   where, $g_a^i(\mathbf{x}, t)$ and $h_\alpha(\mathbf{x}, t)$ are distribution functions at position $\mathbf{x}$ and time t for

2   concentration and temperature, respectively. $g_\alpha^{i(eq)}$ and h_α^{eq} are equilibrium distribution

3   functions for concentration and temperature. ∇C_i and ∇T are the gradients of concentration

4   and temperature, respectively. For the D3Q7 model, $\mathbf{e}_\alpha$, c_s, w_α are given by:

$$\mathbf{e}_0 = (0,0,0),$$

$$\mathbf{e}_1 = (1,0,0), \ \mathbf{e}_2 = (-1,0,0), \ \mathbf{e}_3 = (0,1,0), \tag{21}$$

$$\mathbf{e}_4 = (0,-1,0), \ \mathbf{e}_5 = (0,0,1), \ \mathbf{e}_6 = (0,0,-1)$$

$$c_s = \sqrt{2/7}, \ w_0{=}1/4, \ w_{1\text{-}6}{=}1/8 \tag{22}$$

5   The gradients of concentration (∇C_i) and temperature (∇T) can be calculated by[16-18]:

$$\nabla C_i = -\frac{\sum_a \mathbf{e}_\alpha g_a^i - \sum_a \mathbf{e}_\alpha g_a^{i(eq)}}{c_s^2 \tau_g \Delta t} \tag{23}$$

$$\nabla T = -\frac{\sum_a \mathbf{e}_\alpha h_a - \sum_a \mathbf{e}_\alpha h_a^{eq}}{c_s^2 \tau_h \Delta t} \tag{24}$$

6   The S_i and S_T in the source term, including the effects of the chemical reaction and heat

7   transport can be defined as:

$$S_i = \xi_i R_{meth} \tag{25}$$

$$S_T = \frac{R_{meth} Q_{reaction}}{\rho_{mix} C_{\rho,mix}} \tag{26}$$

8   where R_{meth} is the reaction rate. ξ_i and ρ_{mix} are the stoichiometric coefficient of

9   component i and density of the mixture, respectively. It should be noted that, $Q_{reaction}$ is

10   equal to the reaction heat at the fluid-solid interface, whereas $Q_{reaction}$ is zero at the other

11   place without reaction. The specific heat capacity of the mixture ($C_{\rho,mix}$) can be calculated by

$C_{\rho,mix} = \sum x_i C_{\rho,i}$, here x_i is the mass fraction of component i.

According to the Chapman-Enskog expansions, the mass diffusion coefficient of component i (D_i), the thermal diffusion coefficient of mixture gas ($K_{mix} = \lambda_{mix}/\rho_{mix}C_{p,mix}$), the concentration of component i (C_i), and the temperature (T) can be calculated by the following equations:

$$D_i = c_s^2 \left(\tau_g - \frac{1}{2} - A_i\right)\Delta t \tag{27}$$

$$K_{mix} = c_s^2 \left(\tau_h - \frac{1}{2} - A_T\right)\Delta t \tag{28}$$

$$C_i = \sum_\alpha g_\alpha^i \tag{29}$$

$$T = \sum_\alpha h_\alpha \tag{30}$$

where the values of D_i and K_{mix} are dependent on τ_g, A_i and τ_h, A_T, respectively. The present work keeps τ_g=1 and τ_h=1 to guarantee the stability of the LBM model. Therefore, the values of D_i and K_{mix} are controlled by A_i and A_T, respectively.

Boundary conditions and reaction model

For hydrodynamic boundary conditions, the Zou-He scheme[30] was applied to inlet and outlet boundaries. The solid-fluid interface on porous pellets was regarded as no flux condition. The standard bounce-back scheme was utilized for the no flux boundary condition[31-33]. Regarding the boundary condition of the heat and mass transport process, the non-equilibrium extrapolation scheme proposed by Guo et al.[34] was applied to inlet and outlet boundaries.

For reaction boundary, the empirical kinetic model for the Sabatier process proposed by Takano[35] was used, consisting of individual terms of forwarding reaction and its backward reaction.

$$R_{\mathrm{meth}} = k_f \frac{K_{\mathrm{CO_2}} p_{\mathrm{CO_2}} p_{\mathrm{H_2}}^{0.5}}{\left(1 + K_{\mathrm{CO_2}} p_{\mathrm{CO_2}}\right)^2} - k_r \frac{K_{\mathrm{H_2O}} p_{\mathrm{CH_4}}^2 p_{\mathrm{H_2O}}}{\left(1 + K_{\mathrm{H_2O}} p_{\mathrm{H_2O}}\right)^2} \tag{31}$$

1   where, k_f and k_r represent reaction rate constants of forwarding reaction and backward

2   reaction, respectively, which can be expressed by the Arrhenius equation. K_i and p_i are

3   adsorption equilibrium constant and partial pressure of component i, respectively.

$$k_j = k_{j,0} e^{\left(-\frac{E_{a,j}}{RT}\right)} \tag{32}$$

$$K_i = K_{i,0} e^{\left(-\frac{\Delta H_i}{RT}\right)} \tag{33}$$

4   where $k_{j,0}$ and $K_{i,0}$ stand for the pre-exponential factors. $E_{a,j}$ and ΔH_i are the activation

5   energy and enthalpy change of adsorption, respectively.

6   **Physical Geometry and Code Validation**

7   ***Construction of packing structure***

8   The suitable physical geometry of the packing structure should be determined in advance

9   to implement the simulation. Imaging techniques, such as computed tomography (CT)[37] and

10   magnetic resonance imaging (MRI)[38-39], can give the real experimental images of porous media.

11   However, the required images are probably only valid for specific porous media structures.

12   Moreover, it should be mentioned that even though the high-performance computing

13   techniques can tackle this problem, experimental measurements commonly require many

14   carefully controlled experiments and usually are expensive[40]. For decades, many researchers

15   have developed mathematical algorithms to reconstruct the porous media structure without

16   using experimental images. For example, Adler and Thovert[41] gave a similar porous media

17   structure to the measurements. Concerning the fixed bed's packing structure with abundant

18   randomly distributed catalyst particles, many investigators used the DEM, showing good

1 agreement with the experimental data[41-46]. Therefore, the present simulation adopted the DEM

2 approach to construct the packing structure, following these previous studies. It is noteworthy

3 that three components could control the packing structure, which are the catalyst diameter

4 (d_{cat}), the ratio of the number of inert particles to the number of catalyst particles (N_{inert}/N_{cat}),

5 the inert particle dilution method, respectively. Moreover, the bed porosity (ε) in the DEM

6 approach is implicit. Namely, ε is a given variable after the construction of the packing

7 structure. Plus, the number of catalyst particles (N_{cat}) remains constant in different dilution

8 structures. Fig. 4 shows the schematic diagrams of the packing structure by the DEM approach.

9 *Verification example*

10   Before the code validation, a benchmark example related to the Péclet number for mass

11 transport (Pe_M) based on the Lévêsque solution[47] was carried out to compare the results

12 obtained in the present study with the analytical prediction. As illustrated in Fig. 5(a), a

13 parabolic velocity of fully developed laminar flow was applied for the entire domain.

$$u(y) = -4u_{max}\,y(y - L)/L^2 \tag{34}$$

14 where u_{max} is the axial velocity. A constant concentration (C_0) and zero-flux condition are

15 defined for the inlet and outlet boundary conditions, respectively. Moreover, the upper

16 boundary was set to be nonreactive with a zero-flux condition, and the first-order Henry's

17 adsorption process was applied in the bottom boundary

$$D_F \frac{\partial C}{\partial y} = kC \tag{35}$$

18 where k is the reaction constant.

19   The LKS-LBM model with D2Q5 discrete velocities model was used to calculate the

20 steady-state normalized mass flux (Q) at the bottom for the above process and compare it with

the Lévêsque solution. The correlation of normalized mass flux (Q) obtained by Lévêque[48] and

Machado[49] can be expressed as:

$$Q = \frac{L}{C_0}\frac{\partial C}{\partial \boldsymbol{n}} = 0.854\left(\frac{u_{max}L^2}{xD_F}\right)^{\frac{1}{3}} \tag{36}$$

where x is the streamwise coordinate. The relevant simulation parameters under lattice units

are presented in Table 1. As shown in Fig.5 (b), the present studies show good agreement with

the Lévêsque solution, indicating the accuracy of the LKS-LBM model and physical geometry.

Code validation

The comparison between the present study and experimental data were conducted in this

section. For the sake of simplicity, three dimensionless parameters, Reynolds number (Re),

Péclet number for mass transport (Pe_M), and Péclet number for heat transport (Pe_T), were

adopted to convert the physical unit into lattice units, which can be defined by:

$$Re = \left.\frac{u_{mean}d_{cat}}{v_{mix}}\right|_{LBM} = \left.\frac{u_{mean}d_{cat}}{v_{mix}}\right|_{Physical} = 107 \tag{37}$$

$$Pe_M = \left.\frac{u_{mean}d_{cat}}{D_{H_2}}\right|_{LBM} = \left.\frac{u_{mean}d_{cat}}{D_{H_2}}\right|_{Physical} = 105 \tag{38}$$

$$Pe_T = \left.\frac{u_{mean}d_{cat}\rho_{mix}C_{p,mix}}{\lambda_{mix}}\right|_{LBM} = \left.\frac{u_{mean}d_{cat}\rho_{mix}C_{p,mix}}{\lambda_{mix}}\right|_{Physical} = 228 \tag{39}$$

where u_{mean} and d_{cat} are average velocity in porous media and catalyst diameter,

respectively. Moreover, v_{mix}, $C_{p,mix}$ and λ_{mix} can be calculated by each component:

$$v_{mix} = v_{H_2}x_{H_2} + v_{CO_2}x_{CO_2} + v_{H_2O}x_{H_2O} + v_{CH_4}x_{CH_4} \tag{40}$$

$$C_{p,mix} = C_{p,H_2}x_{H_2} + C_{p,CO_2}x_{CO_2} + C_{p,H_2O}x_{H_2O} + C_{p,CH_4}x_{CH_4} \tag{41}$$

$$\lambda_{mix} = \lambda_{H_2}x_{H_2} + \lambda_{CO_2}x_{CO_2} + \lambda_{H_2O}x_{H_2O} + \lambda_{CH_4}x_{CH_4} \tag{42}$$

where x_i is the mass fraction of component i. Table 2 lists the physical properties of each component concerning NIST. It is noteworthy that these physical properties all depend on the temperature. The relevant input parameters are: $y_{H_2,inlet} = 0.799$, $y_{CO_2,inlet} = 0.199$, $y_{H_2O,inlet} = 0.001$, $y_{CH_4,inlet} = 0.001$, $T_{inlet} = 473\ K$, $C_{sum}=90.182\ mol$ in 0.35 MPa, $C_{sum}=154.598\ mol$ in 0.60 MPa, $C_{sum}=280.854\ mol$ in 1.09 MPa.

As for the Sabatier reaction, Table 3 shows the values of kinetic parameters in the present study. Moreover, the reaction kinetic was based on the powder-like catalyst. Therefore, the reaction rate (R_{geo}) for geometry catalysts in this model should multiply by the scaling factor.

$$R_{geo} = \beta \cdot R_{meth} \tag{43}$$

where β is the scaling factor, which considers the effect of intra-particle transport. In order to further validate the LKS-LBM model, the present study compares the predicted data and experimental data. Regarding the experiment configuration, Fig. 6 shows the schematic diagram of the single shell-and-tube reactor. The length of the reactor is 2000 mm, and the diameter of the reactor tube is 28 mm where the length of the catalyst packed bed at the center of the reactor tube is 1500 mm. The experiment's catalyst is from Hitachi Zosen[59], and thermocouples' positions are on the tubular reactor's central axis. The catalyst pellet is a cylindrical geometry catalyst (diameter: 3 mm; height: 3 mm). Fig. 6 also illustrates the temperature distribution measured on the central axis. The significant temperature variation appears clearly near the inlet.

For the sake of simplicity, the present simulation targets only close to the single tubular reactor's inlet (first 150 mm) for validation. The temperature increasing trend and peak arose in the previous simulation. Moreover, the cylindrical geometry catalysts are simplified into the

sphere geometry catalysts with the same surface area. This section adopts the simulation domain with 500×100×100 (with catalyst particles of diameter 10 lattice points). As shown in Fig. 7 (a), the comparison between the experimental data and predicted results with three scaling factors ($\beta = 0.02$; $\beta = 0.01$; $\beta = 0.005$) in 0.6 MPa. The predicted results show obviously a good agreement with experimental data when $\beta = 0.01$. As presented in Fig. 7 (b), predicted results with $\beta = 0.01$ have a good agreement with experimental data under three different pressures (0.35 MPa, 0.6 MPa, and 1.09 MPa), indicating that the value of the scaling factor ($\beta = 0.01$) is reasonable in this simulation. Moreover, this demonstrates the accuracy of both the physical and mathematical models established in this study.

Results and Discussion

The present simulation adopted the bed dilution to tackle the temperature runaway phenomenon for the Sabatier process, adding inert particles into the catalyst packing structure. Optimizing the temperature distribution in a fixed bed reactor eases the temperature runaway phenomenon. Most relevant researches[1-5] mentioned that the reasonable reaction temperature range for the Sabatier process was 523-823 K. According to the previous studies[2-3], the temperature over 823 K causes catalyst deactivation due to unfavorable sintering and carbon deposition. Therefore, the critical temperature defined here is 800 K, and the present study aims to regulate the peak temperature below this temperature by adding inert particles. Moreover, the predicted carbon conversion rate was used as an indicator to estimate the reaction performance for the Sabatier process. Since the kinetic model in the present study was a one-step model, CO_2 the conversion rate was defined as the carbon conversion rate:

$$X_C = \frac{m_{CO_2,\text{inlet}} - m_{CO_2,\text{outlet}}}{m_{CO_2,\text{inlet}}} \tag{44}$$

1   where $m_{CO_2,\text{inlet}}$ and $m_{CO_2,\text{outlet}}$ denote the inlet and outlet mass flow rates of CO_2,

2   respectively. The present section evaluated the effects of several structural parameters related

3   to bed dilution: the volume fraction of the inert particle ($V_{inert}/V_{inert+cat}$), inert particle

4   dilution method, and inert particle conductivity, respectively. Apart from the discussion about

5   the inert particle conductivity, the material of the inert particle was alumina (Al_2O_3). Moreover,

6   the reaction operating conditions for the Sabatier process were kept constant to explore the

7   relationships between the packing structure and the temperature distribution (inlet temperature:

8    $T = 473.15$ K, operating pressure: $P = 0.6$ MPa, and H_2/CO_2 feed ratio $= 4{:}1$).

9   *Effect of inert particle volume fraction*

10   Since the Sabatier process refers to a strongly exothermic reaction, the present simulation

11   added the inert particles to the catalyst packing structure to regulate the reaction temperature

12   distribution. Taniewski et al.[50] reported that dilution using inert particles provided the lower

13   and wider local temperature peaks (hot-spots) and those shifted to the exit from the bed. The

14   present section analyzed the effect of the inert particle volume fraction on temperature

15   distribution. Fig. 8 presents three types of bed dilution structures exhibiting different inert

16   particle volume fractions under the equal number of catalyst particles. Note that the red and

17   blue particles represent the inert and catalyst ones, respectively, in the mixing dilution method.

18   Moreover, Fig. 9 shows the temperature distributions versus variation of the inert particle

19   volume fraction ($V_{inert}/V_{inert+cat} = 50.0\%, 33.3\%, 16.7\%$).

20   As indicated in Fig. 9, increasing the inert particle's volume fraction limits the temperature

21   distribution. Notably, the predicted peak temperature was lower than the critical temperature

(800 K) set in the present study for $V_{inert}/V_{inert+cat} \geq 33.3\%$. Furthermore, Fig. 8 indicates that with a rise of volume fraction of inert particles, a longer packing structure length is required to maintain the equal number of catalyst particles, which is no economical. Thus, under the volume fraction of inert particles taking up 33.3%, it could control the temperature distribution below the critical temperature (800 K) and reduce the length of the packing structure maximally.

Effect of inert particle dilution method

The inert particle dilution method was also critical to regulating temperature distribution for a strongly exothermal reaction in a fixed bed reactor. Van Den Bleek et al.[58] pointed out that different inert particle distribution would affect the reaction conversion. Hong et al.[14] employed four inert particle dilution methods: without inert particles, inert particles and catalyst in 4 layers, inert particles and catalyst in 8 layers, and catalyst mixed with inert particles. Then, they determined the effect of the dilution method on temperature distribution and reaction conversion rate for Fischer-Tropsch synthesis (FTS). They reported that adding inert particles could effectively control the temperature distribution and increase CO_2 conversion and CH_4 selectivity compared with the case without inert particles. Moreover, the dilution method of catalyst uniformly mixed with inert particles demonstrated superior temperature distribution and reaction conversion to other dilution methods. In this section, the inert particle dilution method was considered for the Sabatier process as well.

First, the mixing dilution method and layered dilution method were investigated. Considered methods were one mixing dilution method (catalyst uniformly mixed with inert particles) and two types of layered dilution method (inert particle and catalyst in 9 layers and inert particle and catalyst in 5 layers). Fig. 10 illustrated the schematic diagrams of the

mentioned dilution methods. Moreover, the number of catalysts in these packing structures is kept constant.

Fig. 11 indicates that the central axis temperature distributions using the dilution methods were lower than the critical temperature (800 K) defined in the present study. Moreover, Figs. 11 and 12 confirmed the reactor bed's unstable temperature profiles using the layered dilution method (inert particles and catalyst in 9 layers and 5 layers). Hong et al.[14] stressed that the unstable temperature profile was due to the different degrees of heat transfer between the catalyst layers, affecting thermal stability in the reactor bed's axial direction. Fig. 13 further exhibits the effect of the unstable temperature profile on reactants and products for the Sabatier process. In terms of the layered dilution method, the mass fractions of reactants (H_2 and CO_2) and products (CH_4 and H_2O) indicated a step-change attributed to an unstable temperature profile. Moreover, in Table 4, the carbon conversion rate in the mixing dilution method (catalyst uniformly mixed with inert particles) was higher than the layered dilution methods, demonstrating that the mixing dilution method could be superior to the layered dilution method.

To gain insights into the effect of the mixing dilution method on temperature distribution and carbon conversion rate, the following three mixing schemes were discussed, i.e., catalyst uniformly mixed with inert particles and two gradient mixing schemes. The two gradient mixing schemes use the heat profile and temperature profile on the central axis without adding inert particles. Namely, the high-temperature place needs more inert particles. For simplicity, the gradient structure based on heat profile is called the first gradient mixing scheme; the gradient structure based on temperature profile is called the second gradient mixing scheme. Fig. 14 illustrates the inert particle volume fraction distribution along the longitudinal direction

for the three mixing schemes. In Fig. 15, the temperature distributions using the three mixing schemes on the central axis are less than that without bed dilution and the critical temperature (800 K). Moreover, the temperature distribution in the first gradient scheme is superior to the other two schemes, and its peak temperature does not exceed 773.15 K. Besides, Fig. 16 further illustrates the optimal reaction performance of the first gradient scheme. The more products (CH_4 and H_2O) yielded due to the superior temperature distribution than those using the other two methods. Table 4 shows the highest carbon conversion rate in the first gradient scheme (65.22%). The improvement in the carbon conversion rate was almost 18% using the inert particle dilution method, compared with the predictions for no bed dilution.

Effect of inert particle conductivity

Different inert particle conductivities probably affect the heat transfer and temperature distribution in the packing structure. This section investigated the effect of inert particle conductivity on temperature distribution for the Sabatier process. Plus, Table 5 lists the thermal conductivities of the two types of inert particles.

Fig. 17 illustrates the effect of thermal conductivity on the central axial temperature distribution. Interestingly, the effect on central axial temperature distribution was trivial, even with the significantly different thermal conductivity.

Several heat transfer behaviors without bed dilution in the present study were first analyzed to elucidate the mentioned phenomenon. The compared results were heat conduction in the fluid phase ($\varepsilon^* k_f$), heat conduction in the solid phase ($(1 - \varepsilon^*)k_{cat}$), longitudinal thermal dispersion (εk_{dis}). Kuwahara et al.[51] and Yang et al.[52] determined the effective porosity (ε^*) and heat dispersion coefficient (k_{dis}) following the equations, respectively:

$$\varepsilon^* = \frac{k_{cat} - k_{stag}}{k_{cat} - k_f} \tag{45}$$

$$\frac{k_{dis}}{k_f} = 0.15 \frac{Pe_T^2}{2.0 + 1.1\, Pe_T^{0.6}/Pr^{0.27}} \tag{46}$$

1   where k_{stag} is the stagnant thermal conductivity, determined by Hsu et al[56].

2   The thermal conductivity counterparts, namely, $\varepsilon^* k_f$, $(1 - \varepsilon^*)k_{cat}$ and εk_{dis}, are

3   presented in Fig. 18 to investigate their relative contributions to the effective thermal

4   conductivity. According to Fig. 18, in the packing structure without inert particles, the

5   longitudinal thermal dispersion's contribution (εk_{dis}) overwhelms the other two ones.

6   Moreover, heat conduction in the fluid phase ($\varepsilon^* k_f$) and longitudinal thermal dispersion (εk_{dis})

7   primarily occurred in the fluid phase. In contrast, heat conduction in the solid ($(1 - \varepsilon^*)k_{cat}$)

8   appeared in the solid phase. Accordingly, without bed dilution, the heat transport contributions

9   in the fluid phase to the effective thermal conductivity were higher than that in the solid phase,

10   demonstrating that heat conduction in the solid phase plays a controlling step.

11   Fig. 19 further gives the schematic diagram of heat transport in the fluid and solid phases

12   considering the bed dilution. As shown in Fig. 19, the solid phase's heat conduction in the solid

13   phase can fall into two parts in addition to the inert particles. I.e., heat conduction in the catalyst

14   and heat conduction in the inert particle. Since the Sabatier reaction occurred in the catalyst,

15   the heat conduction first occurs in the catalyst. Then the heat was transferred to the inert

16   particles or other catalysts. From the above studies, the contribution of heat conduction in the

17   catalyst was minimal. Namely, the catalyst's heat conduction was still a control step, even

18   though the inert particles' thermal conductivities were higher than that of catalysts. Therefore,

19   the temperature distribution did not change with varying the thermal conductivity of inert

particles.

Conclusions

In this study, the discrete element method (DEM) was used to construct the bed dilution structure. Moreover, numerical simulations using the LKS-LBM approach that is appropriate for the condition with a high Péclet number were performed to calculate temperature distribution and carbon conversion rate for the Sabatier process. The effects of three structural parameters in bed dilution on temperature distribution and carbon conversion rate were investigated, which are the volume fraction of inert particles, inert particle dilution method, inert particle conductivity. Based on the results achieved in the present study, three remarks can be sorted as follows:

1) The temperature distribution due to the Sabatier process decreases with increasing the volume fraction of inert particles under the constraint of a constant number of catalysts. However, the reactor's length gets longer. Based on the critical temperature (800 K) set in the present study, the configuration is optimal when the volume fraction of inert particles is equal to 33.3%.

2) In terms of the bed dilution method, the gradient mixing schemes based on the heat profile show superior temperature distribution and a high carbon conversion rate. I.e., the Sabatier process's carbon conversion can be improved by roughly 18%, compared with that without bed dilution.

3) Inert particles' thermal conductivity has a trivial effect on the temperature distribution when the catalyst thermal conductivity mainly limits heat transport.

1   **Acknowledgments**

2   This work was financially supported in part by the Strategic International Research

3   Cooperative Program (SICORP), Japan Science and Technology Agency (JST). The author

4   (YL) acknowledges the support of the China Scholarships Council (Grant Numbers

5   201908320257).

6

7   **Notation**

c_s = lattice sound speed

C = solute concentration, $mol \cdot m^{-3}$

C_{sum} = total concentration, $mol \cdot m^{-3}$

C_ρ = specific heat capacity, $kJ \cdot kg^{-1} \cdot K^{-1}$

d_{cat} = catalyst diameter, m

D = diffusivity, $m^2 \cdot s^{-1}$

$\mathbf{e}_i$ = discrete velocity

E_a = activation energy, $kJ \cdot mol^{-1}$

f = velocity distribution function

g = concentration distribution function

h = temperature distribution function

k = reaction rate constant

K = adsorption equilibrium constant, MPa^{-1}

L = characteristic length in, m

m = mass flow rate, kg/s

M	= transformation matrix
Ma	= Mach number
N	= the number of particles
p	= pressure, MPa
Pe_M	= Péclet number for mass transport
Pe_T	= Péclet number for heat transport
Q	= normalized mass flux
$Q_{rection}$	= reaction heat, $kJ \cdot mol^{-1}$
Re	= Reynolds number
$\mathbf{S}_F$	= diagonal relaxation matrix for fluid flow
T	= temperature, K
u	= velocity tensor, $m \cdot s^{-1}$
U	= characteristic velocity, $m \cdot s^{-1}$
V	= volume, m^3
w_i	= weight coefficient
x	= position tensor in lattice unit
x_i	= mass fraction of component i
y_i	= mole fraction of component i
ΔH	= enthalpy, $kJ \cdot mol^{-1}$

1

2 *Subscripts and superscripts*

α	= discrete velocity direction

cat = catalyst particle

eq = equilibrium state

f = forwarding reaction

i = component i

$inert$ = inert particle

j = component j

$mean$ = average value

mix = mixture

r = reverse reaction

F = fluid

1

2 *Greek letters*

β = scaling factor in Eq. (43)

ρ = density, $kg \cdot m^{-3}$

ε = porosity

λ = thermal conductivity, $W \cdot m^{-1} \cdot K^{-1}$

ν = kinematic viscosity, $m^2 \cdot s^{-1}$

τ = relaxation time

3 **Literature Cited**

4   1.   Jürgensen L, Ehimen EA, Born J, Holm-Nielsen JB. Dynamic biogas upgrading based on

5   the Sabatier process: thermodynamic and dynamic process simulation. *Bioresource*

technology, 2015;178:323-329.

2. Kiewidt L, Thöming J. Predicting optimal temperature profiles in single-stage fixed-bed reactors for CO_2-methanation. *Chemical Engineering Science* 2015;132:59-71.

3. Liu Q, Wang S, Zhao G, Yang H, Yuan M, An X, Zhou H, Qiao Y, Tian Y. CO_2 methanation over ordered mesoporous NiRu-doped $CaO-Al_2O_3$ nanocomposites with enhanced catalytic performance. *International Journal of Hydrogen Energy* 2018;43:239-250.

4. Stangeland K, Kalai D, Li H, Yu Z. CO_2 methanation: the effect of catalysts and reaction conditions. *Energy Procedia* 2017;105:2022-2027.

5. Esa YAM, Sapawe N. A short review on carbon dioxide (CO_2) methanation process. *Materials Today: Proceedings* 2020.

6. Lin J, Ma C, Wang Q, Xu Y, Ma G, Wang J, Wang H, Dong C, Zhang C, Ding M. Enhanced low-temperature performance of CO_2 methanation over mesoporous $Ni/Al_2O_3-ZrO_2$ catalysts. *Applied Catalysis B: Environmental* 2019;243:262-272.

7. Garbarino G, Bellotti D, Finocchio E, Magistri L, Busca G. Methanation of carbon dioxide on Ru/Al_2O_3: catalytic activity and infrared study. *Catalysis Today* 2016;277:21-28.

8. Guilera J, del Valle J, Alarcón A, Díaz JA, Andreu T. Metal-oxide promoted Ni/Al_2O_3 as CO_2 methanation micro-size catalysts. *Journal of CO_2 Utilization* 2019;30:11-17.

9. Falbo L, Visconti CG, Lietti L, Szanyi J. The effect of CO on CO_2 methanation over Ru/Al_2O_3 catalysts: a combined steady-state reactivity and transient DRIFT spectroscopy study. *Applied Catalysis B: Environmental* 2019:256:117791.

10. Garbarino G, Riani P, Magistri L, Busca G. A study of the methanation of carbon dioxide on Ni/Al_2O_3 catalysts at atmospheric pressure. *International Journal of Hydrogen Energy*

2014;39:11557-11565.

11. Vrijburg WL, Garbarino G, Chen W, Parastaev A, Longo A, Pidko EA, Hensen EJ. Ni-Mn catalysts on silica-modified alumina for CO_2 methanation. *Journal of Catalysis* 2020;382:358-371.

12. Kopyscinski J, Schildhauer TJ, Biollaz SM. Production of synthetic natural gas (SNG) from coal and dry biomass-A technology review from 1950 to 2009. *Fuel* 2010;89:1763-1783.

13. Guo Z, Sun Z, Zhang N, Ding M, Shi S. CFD analysis of fluid flow and particle-to-fluid heat transfer in packed bed with radial layered configuration. *Chemical Engineering Science* 2019;197:357-370.

14. Hong GH, Noh YS, Park JI, Shin SA, Moon DJ. Effect of catalytic reactor bed dilution on product distribution for Fischer-Tropsch synthesis over $Ru/Co/Al_2O_3$ catalyst. *Catalysis Today* 2018;303:136-142.

15. Berger RJ, Pérez-Ramırez J, Kapteijn F, Moulijn JA. Catalyst performance testing: Radial and axial dispersion related to dilution in fixed-bed laboratory reactors. *Applied Catalysis A: General* 2002;227(1-2):321-333.

16. Chai Z, Huang C, Shi B, Guo Z. A comparative study on the lattice Boltzmann models for predicting effective diffusivity of porous media. *International Journal of Heat and Mass Transfer* 2016;98:687-696.

17. Xuan YM, Zhao K, Li Q. Investigation on mass diffusion process in porous media based on Lattice Boltzmann method. *Heat and mass transfer* 2010;46(10):1039-1051.

18. Yoshida H, Nagaoka M. Multiple-relaxation-time lattice Boltzmann model for the

convection and anisotropic diffusion equation. *Journal of Computational Physics* 2010;229(20):7774-7795.

19. Chukwudozie C, Tyagi M. Pore scale inertial flow simulations in 3-D smooth and rough sphere packs using lattice Boltzmann method. *AIChE Journal* 2013;59:4858-4870.

20. Li X, Zhang Y, Wang X, Ge W. GPU-based numerical simulation of multi-phase flow in porous media using multiple-relaxation-time lattice Boltzmann method. *Chemical Engineering Science* 2013;102:209-219.

21. Zhang LZ. A lattice Boltzmann simulation of mass transport through composite membranes. *AIChE Journal* 2014;60:3925-3938.

22. Lin Y, Yang C, Wan Z, Qiu T. Lattice Boltzmann simulation of intraparticle diffusivity in porous pellets with macro-mesopore structure. *International Journal of Heat and Mass Transfer* 2019;138:1014-1028.

23. Yang C, Lin Y, Debenest G, Nakayama A, Qiu T. Lattice Boltzmann simulation of asymptotic longitudinal mass dispersion in reconstructed random porous media. *AIChE Journal* 2018;64:2770-2780.

24. He X, Luo LS. Lattice Boltzmann model for the incompressible Navier–Stokes equation. *Journal of Statistical Physics* 1997;88(3):927-944.

25. Holme R, Rothman DH. Lattice-gas and lattice-Boltzmann models of miscible fluids. *Journal of Statistical Physics* 1992;68(3-4):409-429.

26. Sterling JD, Chen S. Stability analysis of lattice Boltzmann methods. *Journal of Computational Physics* 1996;123(1):196-206.

27. Rakotomalala N, Salin D, Watzky P. Miscible displacement between two parallel plates:

BGK lattice gas simulations. *Journal of Fluid Mechanics* 1997;338:277-297.

28. Leconte M, Martin J, Rakotomalala N, Salin D. Pattern of reaction diffusion fronts in laminar flows. *Physical Review Letters* 2003;90(12):128302.

29. Sterling JD, Chen S. Stability analysis of lattice Boltzmann methods. *Journal of Computational Physics* 1996;123:196-206.

30. Zou Q, He X. On pressure and velocity boundary conditions for the lattice Boltzmann BGK model. *Physics of fluids* 1997;9:1591-1598.

31. Jeong N, Choi DH, Lin CL. Estimation of thermal and mass diffusivity in a porous medium of complex structure using a lattice Boltzmann method. *International Journal of Heat and Mass Transfer* 2008;51(15-16):3913-3923.

32. Ginzburg I. Generic boundary conditions for lattice Boltzmann models and their application to advection and anisotropic dispersion equations. *Advances in Water Resources* 2005;28(11):1196-1216.

33. Yoshida H, Nagaoka M. Multiple-relaxation-time lattice Boltzmann model for the convection and anisotropic diffusion equation. *Journal of Computational Physics* 2010;229(20):7774-7795.

34. Guo ZL, Zheng CG, Shi BC. Non-equilibrium extrapolation method for velocity and pressure boundary conditions in the lattice Boltzmann method. *Chinese Physics* 2002;11(4):366-374.

35. Takano H. Development of a Ni/ZrO_2 catalyst for CO_2 methanation (in Japanese). Hokkaido University. 2016.

36. Inamuro T. A lattice kinetic scheme for incompressible viscous flows with heat

transfer. *Philosophical Transactions of the Royal Society of London. Series A: Mathematical, Physical and Engineering Sciences* 2002;360(1792):477-484.

37. Chukwudozie C, Tyagi M. Pore scale inertial flow simulations in 3-D smooth and rough sphere packs using lattice Boltzmann method. *AIChE Journal* 2013;59:4858-4870.

38. Johns ML, Sederman AJ, Bramley AS, Gladden LF, Alexander P. Local transitions in flow phenomena through packed beds identified by MRI. *AIChE Journal* 2000;46:2151-2161.

39. Robbins DJ, El-Bachir MS, Gladden LF, Cant RS, von Harbou E. CFD modeling of single-phase flow in a packed bed with MRI validation. *AIChE Journal* 2012;58:3904-3915.

40. Guibert R, Nazarova M, Horgue P, Hamon G, Creux P, Debenest G. Computational permeability determination from pore-scale imaging: sample size, mesh and method sensitivities. *Transport in Porous Media* 2015;107(3):641-656.

41. Adler PM, Thovert JF. Real porous media: Local geometry and macroscopic properties. *Applied Mechanics Reviews* 1998;51(9):537-585.

42. Das S, Deen NG, Kuipers JAM. A DNS study of flow and heat transfer through slender fixed-bed reactors randomly packed with spherical particles. *Chemical Engineering Science* 2017;160:1-19.

43. Bai H, Theuerkauf J, Gillis PA, Witt PM. A coupled DEM and CFD simulation of flow field and pressure drop in fixed bed reactor with randomly packed catalyst particles. *Industrial & Engineering Chemistry Research*, 2009;48(8):4060-4074.

44. Dong Y, Sosna B, Korup O, Rosowski F, Horn R. Investigation of radial heat transfer in a fixed-bed reactor: CFD simulations and profile measurements. *Chemical Engineering Journal* 2017;317:204-214.

45. Eppinger T, Seidler K, Kraume M. DEM-CFD simulations of fixed bed reactors with small tube to particle diameter ratios. *Chemical Engineering Journal* 2011;166(1):324-331.

46. Volk A, Ghia U, Liu GR. Assessment of CFD-DEM solution error against computational cell size for flows through a fixed-bed of binary-sized particles. *Powder Technology* 2018;325:519-529.

47. Fried JJ, Combarnous MA. Dispersion in porous media. *Advances in Hydroscience* 1971;7:169-282.

48. Lévêque A. Les lois de la transmission de chaleur par convection. Ann. Des. Mines 1928;13:201-239.

49. Machado R. Numerical simulations of surface reaction in porous media with lattice Boltzmann. *Chemical Engineering Science* 2012;69(1):628-643.

50. Taniewski M, Lachowicz A, Skutil K, Czechowicz D. The effect of dilution of the catalyst bed on its heat-transfer characteristics in oxidative coupling of methane. *Chemical Engineering Science* 1996;51(18):4271-4278.

51. Kuwahara F, Yang C, Ando K, Nakayama A. Exact solutions for a thermal nonequilibrium model of fluid saturated porous media based on an effective porosity. *Journal of Heat Transfer* 2011;133(11).

52. Yang C, Nakayama A. A synthesis of tortuosity and dispersion in effective thermal conductivity of porous media. *International Journal of Heat and Mass Transfer* 2010;53(15-16):3222-3230.

53. Wang Q, Yang C, Wang H, Qiu T. Optimization of process-specific catalytic packing in catalytic distillation process: A multi-scale strategy. *Chemical Engineering Science*

2017;174:472-486.

54. Li X, Cai J, Xin F, Huai X, Guo J. Lattice Boltzmann simulation of endothermal catalytic reaction in catalyst porous media. *Applied Thermal Engineering* 2013;50(1):1194-1200.

55. Bohn CD, Scott SA, Dennis JS, Müller CR. Validation of a lattice Boltzmann model for gas-solid reactions with experiments. *Journal of Computational Physics* 2012;231(16):5334-5350.

56. Hsu CT, Cheng P, Wong KW. Modified Zehner-Schlunder models for stagnant thermal conductivity of porous media. *International Journal of Heat and Mass Transfer* 1994;37(17):2751-2759.

57. Lin Y, Yang C, Choi C, Zhang W, Machida H, Norinaga K. Lattice Boltzmann simulation of multicomponent reaction-diffusion and coke formation in a catalyst with hierarchical pore structure for dry reforming of methane. *Chemical Engineering Science* 2021;229(16):116105.

58. Van Den Bleek CM, Van Der Wiele K, Van Den Berg PJ. The effect of dilution on the degree of conversion in fixed bed catalytic reactors. *Chemical Engineering Science* 1969;24(4):681-694.

59. Zhang W, Machida H, Takano H, Izumiya K, Norinaga K. Computational fluid dynamics simulation of CO2 methanation in a shell-and-tube reactor with multi-region conjugate heat transfer. *Chemical Engineering Science* 2020;211:115276.

60. Yang LM, Shu C, Chen Z, Wu J. Three-dimensional lattice Boltzmann flux solver for simulation of fluid-solid conjugate heat transfer problems with curved boundary. *Physical Review E* 2020;101(5):053309.